論文 / 著書情報
Article / Book Information

Title	Impact of MoSe2 Layer on Carrier Transport at the Back Contact in Cu(In,Ga)Se2 Solar Cells
Authors	Yosuke Abe, Takahito Nishimura, Akira Yamada
Citation	IEEE Journal of Photovoltaics, Vol. 15, Issue 1, Page 79-86
Pub. date	2025, 1
DOI	https://doi.org/10.1109/JPHOTOV.2024.3496479
Creative Commons	Information is in the article.

Impact of $MoSe_2$ Layer on Carrier Transport at the Back Contact in Cu(In,Ga)Se_2 Solar Cells

Yosuke Abe, Takahito Nishimura, and Akira Yamada

***Abstract*—This study focuses on the impact of $MoSe_2$ at the Mo/Cu(In,Ga)Se_2 (CIGS) interface on back contact characteristics in CIGS solar cells. The unintentionally formed $MoSe_2$ layer has been reported to establish a quasi-ohmic contact at the Mo/CIGS interface. In this research, we construct a device model for the CIGS solar cells with the $MoSe_2$ intermediate layer using the solar cell capacitance simulator (SCAPS-1D) considering the experimentally measured physical properties. By assuming Mo vacancies as the source of p-type conductivity of $MoSe_2$, we demonstrate the reproducibility of the experimental series resistance. At the Mo/$MoSe_2$ interface, a Schottky barrier of around 0.9 eV for holes is formed due to the difference in their work functions. It is revealed that the quasi-ohmic contact is formed by recombination between holes and electrons through the defect in the $MoSe_2$, despite the Schottky barrier. Since the recombination at the $MoSe_2$ layer follows the SRH model, the density of Mo vacancy significantly reduces the series resistance. Meanwhile, the decrease in the series resistance by the increase in the Mo vacancy saturates at around 0.83 $\Omega{\cdot}cm^2$. To further reduce series resistance, Nb doping into the $MoSe_2$ is proposed in SCAPS-1D, enhancing p-type conductivity. It is disclosed that the Nb doping induces a transition in dominant hole transport from recombination toward tunneling, resulting in a decrease in the series resistance. If the doping density of the Nb exceeds 5 $\times$ 1019 cm^{-3}, the series resistance becomes comparable to the flat band condition of the back contact.**

***Index Terms*—Back contact, $MoSe_2$, quasi-ohmic contact, thin-film Cu(In,Ga)$(Se,S)_2$ solar cell.**

I. Introduction

CU(In,Ga)Se_2 (CIGS) is one of the most promising materials as a light-absorbing layer in thin-film solar cells, characterized by a high optical absorption coefficient and a tunable bandgap (E_g) (1.00–1.68 eV) [1]. The power conversion efficiency (PCE) of 23.6% [2] has been achieved in lab-scale cells by improving CIGS bulk properties and buffer layer interface characteristics [2], [3], [4]. However, the increase in efficiency has slowed down in recent years, and analysis of the back contacts is needed to further improve efficiency. Recently, an analysis focusing on transparent conducting oxide (TCO) has been conducted to assess the impact of series resistance (R_s) [5]. Similarly, the back contact resistance also affects the properties of the CIGS solar cells. Poor contact characteristics lead to the distortion of a current density–voltage (J–V) curve, such as rollover, kink, and an increase in R_s [6], [7], [8], [9], [10].

Generally, Mo is used as the back contact material in the CIGS solar cells because of its low electrical resistivity and high stability at high temperatures. Mo reacts with Se during the high-temperature growth of the CIGS absorption layer [11], forming a $MoSe_2$ layer at the Mo/CIGS interface. $MoSe_2$ belongs to the VI-group transition metal dichalcogenides and has a hexagonal structure with sheets composed of Se–Mo–Se covalent bonds held together by weak van der Waals forces [12]. In the CIGS solar cells, the orientation and electrical properties of $MoSe_2$ have been found to be affected by various factors, including the sputtering conditions of Mo, the alkali content from the glass, and the film formation conditions of CIGS [13], [14], [15]. It has been suggested that $MoSe_2$ alleviates the Schottky barrier expected from the work functions of CIGS and Mo, forming a quasi-ohmic contact [9], [15]. However, the mechanism of the quasi-ohmic contact and the carrier transport have not been discussed in detail. In this regard, we constructed a device model of the CIGS solar cell based on actual measurements and analyzed the effect of the $MoSe_2$ layer on the backside characteristics by theoretical calculations using solar cell capacitance simulator (SCAPS-1D) [16]. In addition, to reduce the resistance loss at the back contact for the CIGS solar cells, we analyzed the effect of Nb doping [17], [18], [19] into the $MoSe_2$ layer, where the Nb element acts as an acceptor. The usefulness of the highly doped p-type $MoSe_2$ intermediate layer is theoretically discussed.

II. Simulation Methodology

To experimentally obtain the physical properties of the actual devices, the CIGS solar cell with SLG (soda-lime glass)/Mo/CIGS/CdS/i-ZnO/ZnO:B/Al structure was prepared. Mo was formed on the SLG by direct current (dc) sputtering. The CIGS layer was then grown by a three-stage process [20] using a molecular beam epitaxy system. The solar cell was completed with CdS as n-type buffer deposited by chemical-bath deposition, i-ZnO as a high-resistance buffer, ZnO:B as a window layer deposited by metal-organic chemical vapor deposition, and Al finger electrode by thermal evaporation. Fig. 1 shows the J–V characteristic for the completed CIGS solar cells. The PCE, open-circuit voltage (V_{oc}), short-circuit current density (J_{sc}), fill factor (FF), R_s, and shunt resistance (R_{sh}) are summarized in Table I.

Received 26 January 2024; revised 17 October 2024; accepted 8 November 2024. This work was supported by the New Energy and Industrial Technology Development Organization (NEDO). *(Corresponding author: Yosuke Abe.)*

The authors are with the Department of Physical Electronics, Institute of Science Tokyo, Tokyo 152-8550, Japan (e-mail: abe.y.bc@m.titech.ac.jp; nishimura.t.ak@m.titech.ac.jp; yamada.a.ac@m.titech.ac.jp).

This article has supplementary material provided by the authors and color versions of one or more figures available at https://doi.org/10.1109/JPHOTOV.2024.3496479.

Digital Object Identifier 10.1109/JPHOTOV.2024.3496479

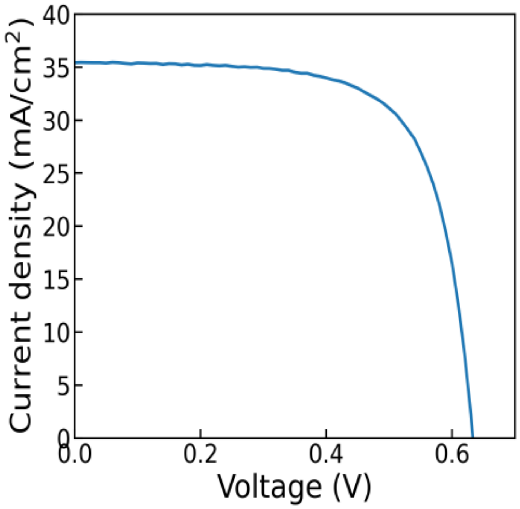

Fig. 1. *J–V* curve of the CIGS solar cell on which the simulation was based.

TABLE I
SOLAR CELL CHARACTERISTICS OF FIG. 1

PCE (%)	V_{oc} (V)	J_{sc} (mA.cm^{-2})	FF	R_s (Ω.cm^2)	R_{sh} (Ω.cm^2)
15.6	0.633	35.4	0.696	0.968	1214

PCE, *V*oc, *J*sc, FF, *R*s, and *R*sh are power conversion efficiency, open-circuit voltage, short-circuit current density, fill factor, series resistance, and shunt resistance, respectively.

The simulation parameters for each layer are listed in Table II. The E_g and electron affinity (χ) of the CIGS layer were estimated using the reported equations as a function of the Ga/(Ga+In) ratio [21] inferred from first-principles calculations. The compositional ratio in the depth direction for the CIGS layer was obtained from energy-dispersive X-ray (EDX) spectroscopy as shown in Fig. S1 in Supplementary Material. A Cu-deficient layer (CDL) is known to be formed on the surface of CIGS prepared by the three-stage method, and the decrease in Cu concentration causes a shift of the valence band maximum (VBM) to the lower energy side [22], [23]. The χ of CDL was adjusted to that of the CIGS surface, and the VBM reduction was taken into account by increasing the E_g by 0.1 eV from the CIGS surface value [24]. Table III shows the defect properties for the CIGS layer and CDL assuming the antisite defect of In_{Cu}. The total defect density was adjusted to coincide with the experimental V_{oc} for the CIGS solar cell.

The thickness of the $MoSe_2$ layer was estimated from the cross-sectional transmission electron microscope (TEM) image of the CIGS solar cell in Fig. 2. The c-axis oriented $MoSe_2$ with a thickness of approximately 5 nm was observed at the Mo/CIGS interface. It has been experimentally and theoretically disclosed that $MoSe_2$ is an indirect transition semiconductor with an E_g of about 1.09 eV [25], [26]. The χ of $MoSe_2$ was set to 4.43 eV based on the analysis of the band structure of $MoSe_2$ by UV photoelectron spectroscopy and inverse photoemission spectroscopy after the liftoff of a CIGS film on Mo [27]. The carrier type of $MoSe_2$ has been discussed in various ways [17], [28], [29], [30], [31]. When the $MoSe_2$ is assumed as n-type

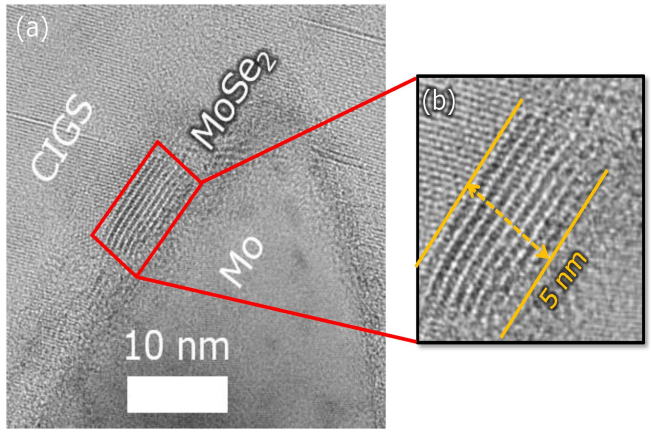

Fig. 2. (a) Cross-sectional TEM images at the back contact of the CIGS solar cell. (b) Magnified image enclosed by red rectangle.

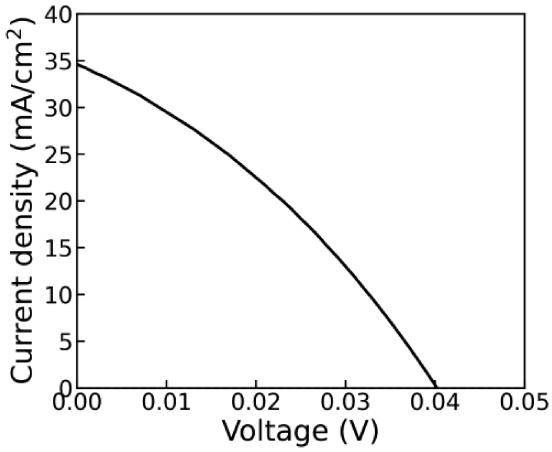

Fig. 3. *J–V* curve when assuming n-type $MoSe_2$ due to Se vacancy (V_{Se}). The donor defect of 1×10^{17} cm^{-3} due to V_{Se} at 0.1 eV below the conduction band minimum and the neutral defect of 5×10^{20} cm^{-3} in the middle gap as a recombination center were introduced, respectively.

conductivity due to Se vacancy, the device characteristics were very poor and the experimental data could not be reproduced in the simulation as shown in Fig. 3. In this article, we, therefore, assumed a p-type $MoSe_2$ layer. For the origin of the p-type, Mo vacancy (V_{Mo}) [32], [33] was assumed as a native defect and its electrical characteristics are shown in Table IV. It has been reported that Mo vacancies in monolayer $MoSe_2$ form defect levels with an extension near the middle gap [34]. Hence, the defect state with Gaussian distribution was introduced at a depth of 0.5 eV above the VBM. Fig. 4 shows the band diagram near the back contact (a) before and (b) after the formation of the junction in thermal equilibrium state. The hole barrier of about 0.9 eV is formed at the Mo/$MoSe_2$ interface, and the conductivity of the $MoSe_2$ near Mo changes from p-type to n-type due to strong band bending.

III. RESULTS AND DISCUSSION

A. R_s and Current Flow at the Back Contact

The back contact characteristics are significantly affected by the hole transport. The R_s is an indicator for the evaluation

TABLE II
PARAMETERS OF EACH LAYER OF THE CIGS SOLAR CELL USED IN SCAPS-1D SIMULATION

Parameter / Material	$MoSe_2$	$Cu(In_{1-x},Ga_x)Se_2$	CDL	CdS	i-ZnO	ZnO:B
W (nm)	5	2000	100	50	50	2000
E_g (eV)	1.09	$0.19x^2 + 0.47x + 1.03$[21]	1.23	2.4	3.3	3.5
χ (eV)	4.43	$-0.16x^2 - 0.50x + 4.55$[21]	4.48	4.2	4.4	4.4
ε_r	7.29	13.6	13.6	10	9	10
N_C (cm^{-3})	9×10^{18}	2.2×10^{18}	2.2×10^{18}	1×10^{19}	1×10^{19}	1×10^{19}
N_V (cm^{-3})	9×10^{18}	1.8×10^{19}	1.8×10^{19}	1×10^{19}	1×10^{19}	1×10^{19}
μ_n (cm^2/Vs)	50	50	50	50	50	50
μ_p (cm^2/Vs)	50	10	10	50	50	50
N_D (cm^{-3})	0	0	1×10^{13}	1×10^{17}	1×10^{19}	1×10^{20}
N_A (cm^{-3})	0	1×10^{16}	0	0	0	0

W and εr are film thickness and dielectric permittivity, N_C and N_V are effective density of states in conduction and valence bands, respectively, μ_n and μ_p are electron and hole mobility, respectively, and N_D and N_A are donor and acceptor density, respectively. The Eg and χ for the CIGS layer were calculated from [21] based on the composition ratios obtained from EDX in the depth direction as shown in Fig. S1 in Supplementary Material.

TABLE III
PARAMETERS RELATED TO DEFECTS IN THE CIGS LAYER AND CDL USED IN SCAPS-1D SIMULATION

Parameter / Material	CIGS	CDL
Defect type	Single donor	Single donor
Total defect density, $N_{In_{Cu}}$ (cm^{-3})	7×10^{14}	3×10^{15}
σ_n (cm^2)	1×10^{-14}	1×10^{-14}
σ_p (cm^2)	1×10^{-14}	1×10^{-14}
Energetic distribution	Gaussian	Gaussian
Energy level with respect to VBM (eV)	0.8	0.8
Characteristic energy, E_c (eV)	0.1	0.1

σ_n and σ_p are capture cross sections of electrons and holes, respectively. Characteristic energy (Ec) is the variance of the Gaussian distribution.

TABLE IV
DEFECT PROPERTIES OF MO VACANCY (V_{Mo}) IN THE $MoSe_2$ LAYER USED IN SCAPS-1D SIMULATION

Defect type	Single acceptor
Total defect density, $N_{V_{Mo}}$(cm^{-3})	Variable
σ_n (cm^2)	1×10^{-10}
σ_p (cm^2)	1×10^{-10}
Energetic distribution	Gaussian
Energy level with respect to VBM (eV)	0.5
Characteristic energy, E_c (eV)	0.1

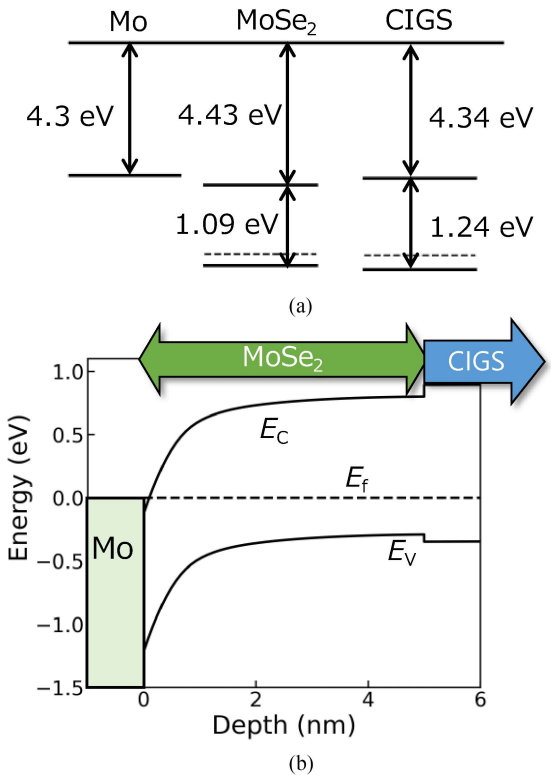

Fig. 4. Band diagram near the back contact (a) before and (b) after the formation of the junction in thermal equilibrium state. E_C, E_V, and E_f are energy levels of the conduction band, valence band, and fermi energy, respectively. The work function of polycrystalline Mo has been reported to be 4.3 eV [35].

of the contact characteristics. Fig. 5 depicts the experimental and theoretical J–V characteristics and Table V shows their R_s values. Two theoretical J–V curves were drowned by the simulation. First, the ideal flat band condition without the $MoSe_2$ layer was simulated, assuming the ideal metal back contact, where the work function of the metal is adjusted to that of CIGS. Second, the $MoSe_2$ intermediate layer with the density of V_{Mo} ($N_{V_{Mo}}$) of 5×10^{20} cm^{-3} was inserted between Mo

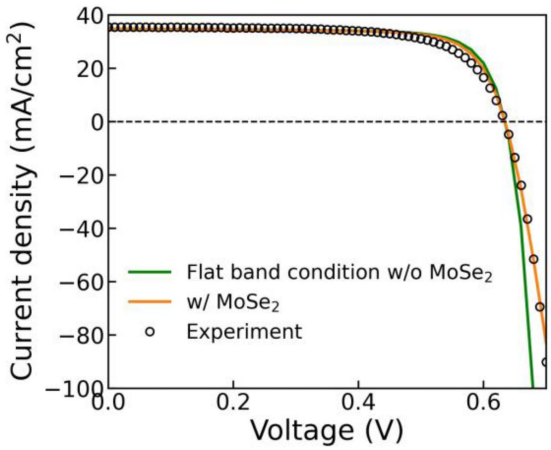

Fig. 5. Experimental and theoretical J–V curve. Two theoretical J–V curves were calculated by SCAPS-1D. The green solid line is the ideal flat band condition where the work function of the metal is adjusted to that of CIGS. The orange solid line is the case where $MoSe_2$ intermediate layer with the density of V_{Mo} ($N_{V_{Mo}}$) of 5×10^{20} cm^{-3} is inserted between Mo and CIGS.

TABLE V
R_s OBTAINED FROM THE J–V CURVE IN FIG. 5

Condition		R_s (Ω.cm^2)
Experiment		0.97
SCAPS-1D	Flat band condition w/o $MoSe_2$	0.41
	w/ $MoSe_2$	0.93

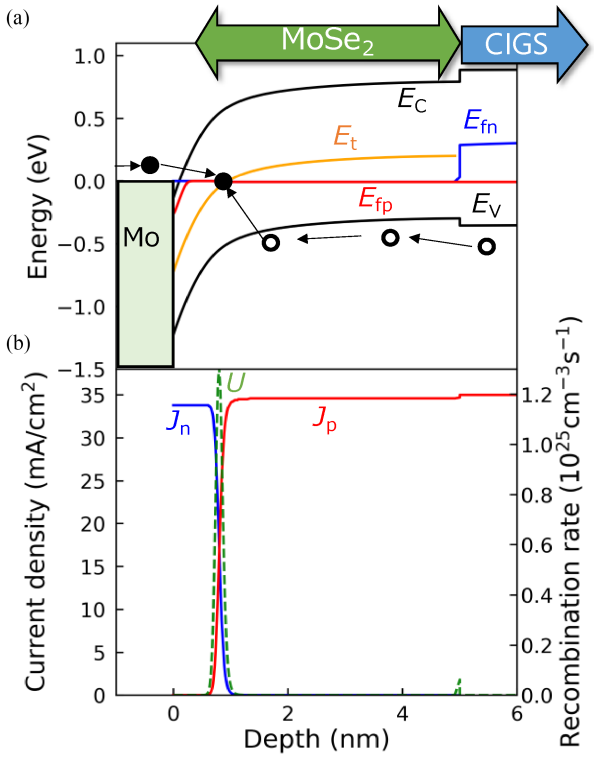

Fig. 6. (a) Band diagram (E_t is the defect level due to V_{Mo}, and E_{fn} and E_{fp} are the quasi-fermi levels of electrons and holes, respectively). (b) Distribution of current density (J_n: electron current dentiy, J_p: hole current density) and recombination rate (U) near the back contact at $V = 0$ V under light irradiation.

and CIGS. The simulated R_s value of 0.41 Ω·cm^2 for the ideal flat band condition was less than half of the experimental R_s of 0.97 Ω·cm^2. Meanwhile, the R_s value of 0.93 Ω·cm^2 for the simulated condition with the $MoSe_2$ intermediate layer was in good agreement with the experimental R_s value.

We focused on the current flow near the back contact in the presence of the $MoSe_2$. Fig. 6 shows (a) the band diagram and (b) the distribution of current density and recombination rate (U) near the back contact at $V = 0$ V under light irradiation. In SCAPS-1D, the current passing through the heterointerface is represented by thermionic emission and tunneling based on the WKB approximation [36], [37]. A large Schottky barrier of about 0.9 eV is formed at the interface between Mo and $MoSe_2$. The hole current density (J_p) rapidly reduced to 0 mA/cm^2 at the depth of $\sim$1 nm from the interface with Mo layer, whereas the J_p was replaced with the electron current density (J_n) through the carrier recombination in the $MoSe_2$ intermediate layer. The integrated U at the depth of $\sim$1 nm in $MoSe_2$ layer corresponds to the total current density value. In other words, at the interface between Mo and $MoSe_2$, the holes flow through the Schottky barrier not by the thermionic emission but by the recombination with electrons coming from the Mo side via defect levels due to V_{Mo}, forming the quasi-ohmic contact. The tunneling current density for the holes from $MoSe_2$ to Mo was on the order of 10^{-20} mA/cm^2, while having almost no impact on the total current. The band diagram of the entire solar cell and the distribution of the current density are shown in Fig. S2 in Supplementary Material, where the photoexcited electrons in the CIGS layer flow to the n-type CdS buffer layer, while the holes flow toward the Mo back contact by carrier recombination.

B. Mo Vacancy Density ($N_{V_{Mo}}$) in the $MoSe_2$ Layer

1) Effect of $N_{V_{Mo}}$ on R_s: As mentioned above, the holes flow at the $MoSe_2$ layer by recombining with electrons through the defect states. Therefore, the dependence of $N_{V_{Mo}}$ in the $MoSe_2$ layer on R_s was investigated to clarify the effect of the defect property in the $MoSe_2$ layer on the back contact characteristics for the CIGS solar cells. Fig. 7 shows the variation of J–V curves with respect to $N_{V_{Mo}}$. The inset in Fig. 7 is a magnified view near the maximum power point. It was revealed that the current density was reduced by decreasing $N_{V_{Mo}}$. This means that the decrease in $N_{V_{Mo}}$ reduces the recombination current density (J_U) in the $MoSe_2$ layer, affecting FF and PCE with increasing R_s. Fig. S3 in Supplementary Material depicts the (a) PCE, (b) FF, (c) V_{oc}, and J_{sc} as a function of $N_{V_{Mo}}$. There was no significant change in V_{oc} and J_{sc}, whereas FF was increased with increasing $N_{V_{Mo}}$, improving the PCE. Fig. 8 shows the variation in J_U and R_s with $N_{V_{Mo}}$. Here, J_U was obtained by integrating the U which exhibits a peak as shown in Fig. 6(b) at $V = 0.6$ V under the light irradiation. The R_s value was decreased with increasing J_U at $N_{V_{Mo}}$ of 4×10^{20} cm^{-3} or below. Meanwhile, the R_s value was saturated to around 0.83 Ω·cm^2 when $N_{V_{Mo}}$ exceeded

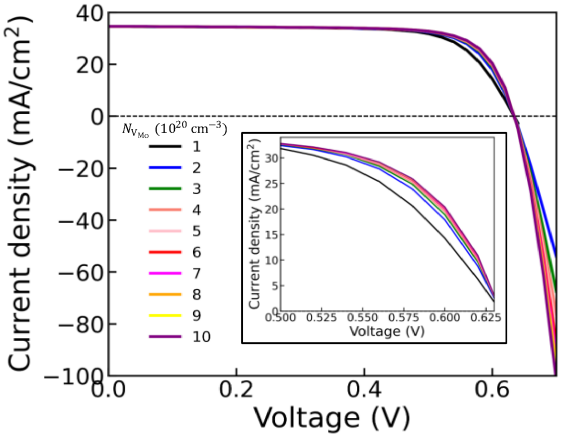

Fig. 7. Variation of *J*–*V* curves with respect to $N_{V_{Mo}}$. The inset shows a magnified view near the maximum power point.

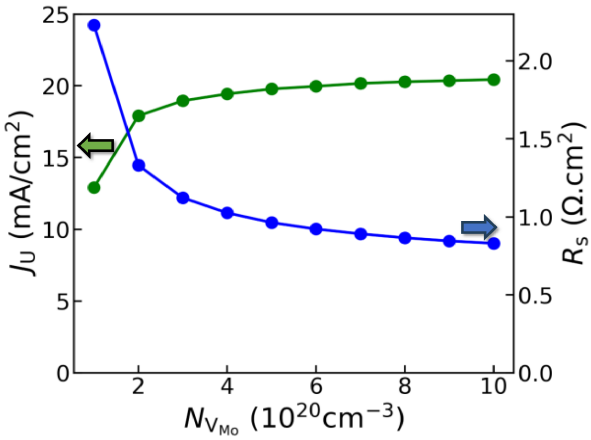

Fig. 8. Variation of J_U and R_s with respect to $N_{V_{Mo}}$. J_U was calculated from the U of the back contact at $V = 0.6$ V under the light irradiation.

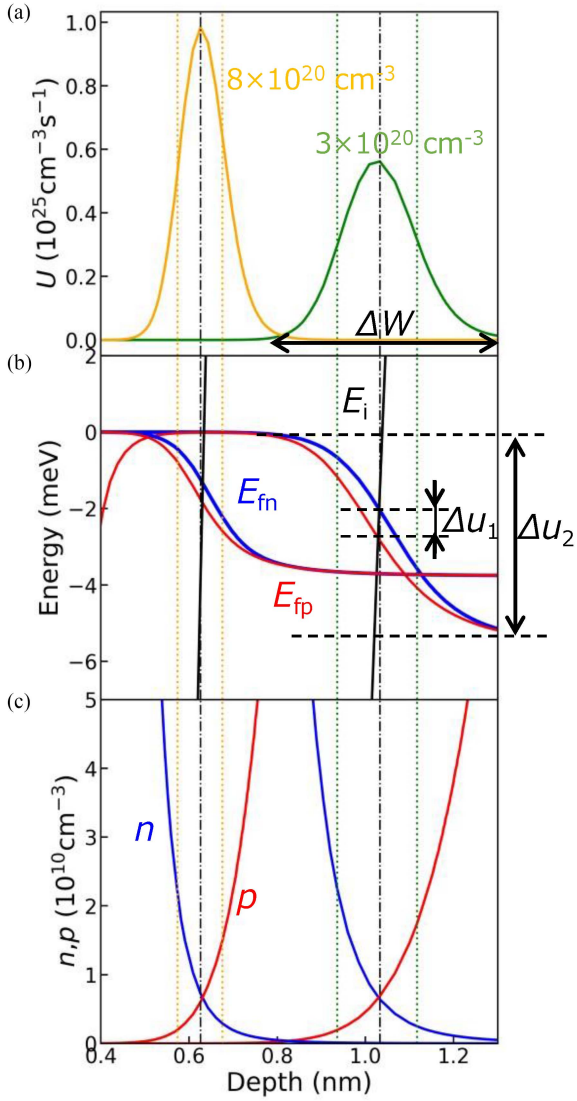

Fig. 9. (a) U, (b) quasi-fermi level of electron (E_{fn}) and hole (E_{fp}), middle gap energy (E_i), and (c) n, p in the depth direction within the $MoSe_2$ layer from the interface with Mo when $N_{V_{Mo}}$ is 8 and 3×10^{20} cm^{-3} at $V = 0.6$ V under the light irradiation with the dashed-dotted line on the center indicating the peak position of the U and the two dotted lines on both sides indicating the FWHM of the U.

4×10^{20} cm^{-3}. Finally, PCE and FF were improved with reducing the R_s (Supplemetary Material Fig. S3), suggesting the usefulness of defect property for the $MoSe_2$ intermediate layer.

2) Theoretical Calculation of the Back Contact Resistance: In this section, the factors to saturate the J_U and back contact resistance are discussed. The recombination at the $MoSe_2$ intermediate layer is the SRH recombination through the defect levels due to V_{Mo}, which can be expressed by the following equation:

$$U = \frac{\sigma_n \sigma_p v_{th} \left(np - n_i^2\right) N_{V_{Mo}}}{\sigma_n \left(n + n_i \exp\left(\frac{E_t - E_i}{kT}\right)\right) + \sigma_p \left(p + n_i \exp\left(-\frac{E_t - E_i}{kT}\right)\right)}. \quad (1)$$

In (1), σ_n and σ_p represent the capture cross sections of electrons and holes, v_{th} is the thermal velocity, n and p are the densities of electrons and holes, n_i is the intrinsic carrier density, E_i is the mid-gap energy, k is the Boltzmann constant, and T is the temperature. From (1), the origin of the J_U saturation in spite of increasing $N_{V_{Mo}}$ is caused by the np product. Fig. S4 in Supplementary Material depicts the (a) U and (b) $(np)^{0.5}$ in the depth direction at the $MoSe_2$ layer from the interface with Mo at $V = 0.6$ V under the light irradiation. Fig. S4(a) in Supplementary Material revealed that the peak width of U decreased with increasing $N_{V_{Mo}}$. This is due to the decrease in the peak width of the $(np)^{0.5}$ shown in Fig. S4(b) in Supplementary Material.

Fig. 9 shows (a) U, (b) quasi-fermi level of electron (E_{fn}), and hole (E_{fp}), middle gap energy (E_i), and (c) n,p when $N_{V_{Mo}}$ is 8 and 3×10^{20} cm^{-3} with the dashed-dotted line on the center indicating the peak position of the U and the two dotted lines on both sides indicating the FWHM of the U.

Fig. 9(b) shows a magnified view of the quasi-Fermi near the carrier inversion, indicating that a slight separation of E_{fn} and E_{fp} is important for SRH recombination. Up to this point, R_s has been used to represent the series resistance of the entire solar cell. However, to focus on the resistance value of the back

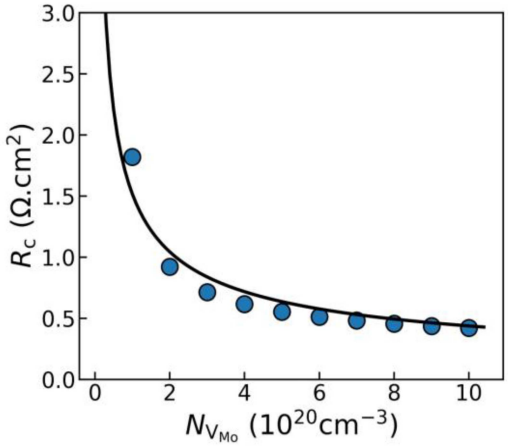

Fig. 10. Relationship between $N_{V_{Mo}}$ and R_c indicated by the blue marker which is estimated from the R_s of the entire solar cell minus the ideal flat band condition where the work function of the metal is adjusted to that of CIGS (see Table V, 0.41 Ω·cm^2). The solid black line is the result of fitting using (2).

contact, we define the back contact resistance (R_c) as the value obtained by subtracting the ideal flat-band condition, where the metal work function is adjusted to match the work function of CIGS (see Table V, 0.41 Ω·cm^2), from the overall R_s of the solar cell.

The relationship between back contact resistance (R_c) and $N_{V_{Mo}}$ is derived by combining Fig. 9 and (1). As discussed in the Supplementary Material (S1)–(S9), R_c can be expressed as

$$R_c = \frac{1}{qn_i\sqrt{\frac{q\mu v_{th}\sigma}{28BkT}}}\frac{1}{\sqrt{N_{V_{Mo}}}} = AN_{V_{Mo}}^{n}. \quad (2)$$

The R_c value decreases in inverse proportion to the square root of $N_{V_{Mo}}$ according to (2), assuming that the current is dominated by SRH recombination in the Schottky contact. A is a constant value determined by physical properties other than $N_{V_{Mo}}$, and n is a multiplier of $N_{V_{Mo}}$. Fig. 10 shows the relationship between R_c and $N_{V_{Mo}}$. The A and n values in (2) were determined by fitting the simulation values shown in Fig. 10. The n was –0.52, which is close to the theoretical value of –0.5. These results indicate that the R_c is determined by the concentration of the recombination center when the hole transport is dominated by the carrier recombination at the $MoSe_2$ layer.

C. Investigation of Nb Doping in $MoSe_2$ Layer

As described above, the decrease in R_s with $N_{V_{Mo}}$ saturates if hole transport is governed by the carrier recombination. To further reduce R_s, $MoSe_2$ should have highly doped p-type conductivity to generate a tunneling current. Nb doping is considered as a promising method to improve the p-type conductivity for the $MoSe_2$ intermediate layer. It has been reported that high acceptor densities exceeding 1×10^{19} cm^{-3} for $MoSe_2$ have been achieved by Nb doping [18]. Furthermore, in previous studies, Nb-doped $MoSe_2$ was formed at the Mo/CIGS interface by sputtering Mo-Nb precursor onto Mo followed by CIGS deposition, leading to a reduction in the series resistance of the solar cells [38].

TABLE VI
DEFECT PROPERTIES OF Nb_{Mo} IN THE $MoSe_2$ LAYER USED IN SCAPS-1D SIMULATION

Defect type	Single acceptor
Defect density, $N_{Nb_{Mo}}$ (cm^{-3})	Variable
σ_n (cm^2)	1×10^{-15}
σ_h (cm^2)	1×10^{-15}
Energetic distribution	Single level
Energy level with respect to VBM (eV)	0.1

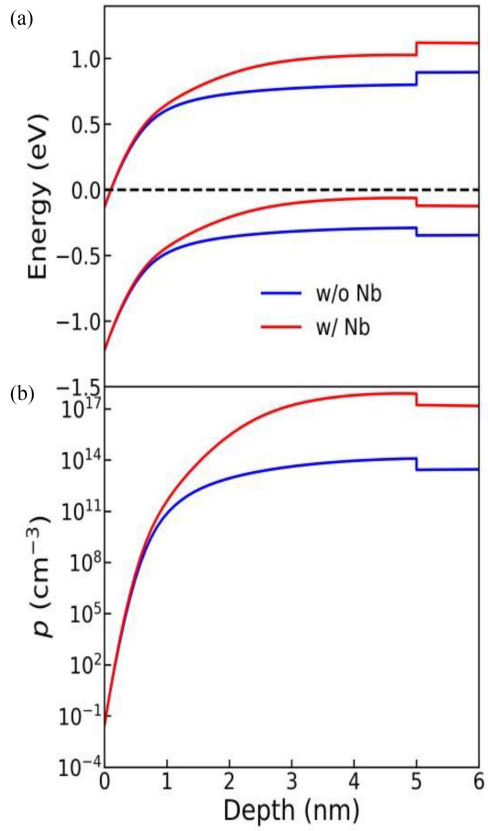

Fig. 11. (a) Band diagram and (b) p in thermal equilibrium in the depth direction from the Mo/$MoSe_2$ interface when Nb doping is applied. $N_{V_{Mo}}$ is 5×10^{20} cm^{-3} for w/o Nb, and $N_{V_{Mo}}$ and N_{NbMo} are 4.5×10^{20} cm^{-3} and 5×10^{19} cm^{-3} for w/ Nb, respectively.

To verify the effect of highly doped p-type $MoSe_2$ on the back contact properties, the model for the antisite defects of Nb on the Mo sites (Nb_{Mo}) which acts as an acceptor in $MoSe_2$ was constructed on SCAPS-1D. It has been reported that the acceptor level due to Nb is relatively shallow in $MoSe_2$ [39]. We hence introduced Nb_{Mo} with a defect energy level at 0.1 eV above the VBM, as shown in Table VI. $N_{V_{Mo}}$ was assumed to be decreased by the formation of N_{NbMo}, where Nb occupies the Mo vacancy. Fig. 11 shows (a) the band diagram and (b) the p in thermal equilibrium when Nb doping is applied. The introduction of a shallow acceptor defect, N_{NbMo}, increased p by more than four orders of magnitude and strongly bended the band.

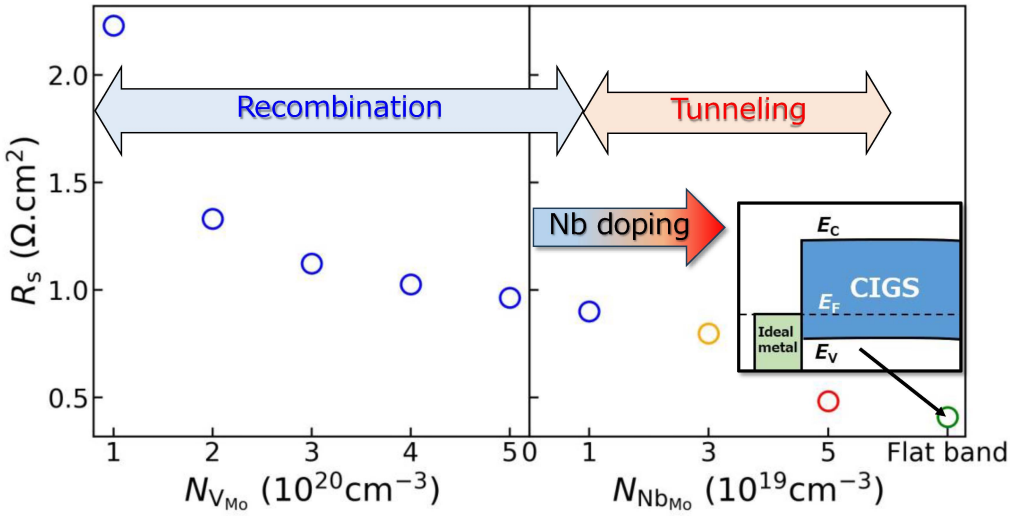

Fig. 12. Variation of R_s with respect to $N_{V_{Mo}}$ and N_{NbMo}.

Fig. 12 shows the variation of R_s with respect to $N_{V_{Mo}}$ and N_{NbMo}. The reduction of R_s was saturated in $N_{V_{Mo}}$ above 4×10^{20} cm^{-3} when the hole transport is dominated by recombination as discussed in Fig. 8. Meanwhile, the R_s value further decreased by introducing N_{NbMo} and finally reached to 0.48 Ω·cm^2 at N_{NbMo} of 5×10^{19} cm^{-3}, which is comparable to that of 0.41 Ω·cm^2 in the ideal flat band condition. Eventually, in Fig. S5(a), (b) in Supplementary Material, FF and PCE were improved due to the lower R_s caused by Nb doping. This result can be explained by the hole tunneling current density (J_{pt}). When N_{NbMo} was 1×10^{19} cm^{-3} and 3×10^{19} cm^{-3}, the J_{pt} was 3.25×10^{-20} mA/cm^2 and 3.61 mA/cm^2, respectively, indicating that the dominant process of hole transport is by recombination. On the other hand, when N_{NbMo} was increased to 5×10^{19} cm^{-3}, the J_{pt} was 22 mA/cm^2, which is a large fraction of the total current of 34.7 mA/cm^2, and tunneling is the dominant process of hole transport. These results show that Nb doping promotes the tunneling of holes from $MoSe_2$ to Mo, resulting in lowering the R_s.

IV. Conclusion

In this study, the effect of $MoSe_2$ at the Mo/CIGS interface on the back contact characteristics was analyzed using SCAPS-1D. TEM measurements confirmed the presence of approximately 5 nm thick $MoSe_2$ at the interface between the Mo and the CIGS layer fabricated using the three-stage process. The introduction of $MoSe_2$ as a p-type semiconductor, attributed to Mo vacancies, in SCAPS-1D successfully reproduced the series resistance of the actual device. At the Mo/$MoSe_2$ interface, a significant Schottky barrier of around 0.9 eV is formed for holes due to the difference in their work functions. However, instead of thermionic emission over this barrier, holes maintain the total current by recombining with electrons coming from the Mo side through the defect level of the Mo vacancies. It has become evident that Mo vacancies, deep-level defects within $MoSe_2$, act as recombination centers, forming a quasi-ohmic contact. Since recombination at the $MoSe_2$ layer is SRH recombination, the density of Mo vacancies has a significant impact on the series resistance. However, the decrease in series resistance due to an increase in Mo vacancy density saturated at approximately 0.83 Ω·cm^2. The relationship between back contact resistance and Mo vacancy density derived from the SRH recombination equation fits the simulation results well, showing that when hole transport is dominated by recombination in Schottky contacts, the contact resistance decreases inversely in proportion to the square root of the Mo vacancy density.

To achieve further reduction in series resistance, Nb doping was proposed into $MoSe_2$ and its effect was also simulated by SCAPS-1D. Nb forms antisites with Mo, improving p-type conductivity in $MoSe_2$ as acceptor defects. As a result, by doping with 5×10^{19} cm^{-3} of Nb, dominant hole transport was transformed from recombination into tunneling, reducing series resistance to the value close to the ideal flat band condition where the work function of the metal is adjusted to that of CIGS, and the efficiency improvement was achieved.

Acknowledgment

The authors would like to acknowledge Dr. Marc Burgelman, University of Gent, Belgium, for providing Solar Cell Capacitance Simulator.

References

[1] T. Maeda, R. Nakanishi, M. Yanagita, and T. Wada, "Control of electronic structure in Cu(In, Ga)(S, Se)$_2$ for high-efficiency solar cells," *Jpn. J. Appl. Phys.*, vol. 59, Apr. 2020, Art. no. SGGF12, doi: 10.35848/1347-4065/ab69e0.

[2] J. Keller et al., "High-concentration silver alloying and steep back-contact gallium grading enabling copper indium gallium selenide solar cell with 23.6% efficiency," *Nature Energy*, vol. 9, no. 4, pp. 467–478, Apr. 2024, doi: 10.1038/s41560-024-01472-3.

[3] K. F. Tai, R. Kamada, T. Yagioka, T. Kato, and H. Sugimoto, "From 20.9 to 22.3% Cu(In,Ga)(S,Se)$_2$ solar cell: Reduced recombination rate at the heterojunction and the depletion region due to K-treatment," *Jpn. J. Appl. Phys.*, vol. 56, 2017, Art. no. 8S2, doi: 10.7567/JJAP.56.08MC03.

[4] Y. Sun et al., "Review on alkali element doping in Cu(In,Ga)Se_2 thin films and solar cells," *Engineering*, vol. 3, no. 4, pp. 452–459, Aug. 2017, doi: 10.1016/J.ENG.2017.04.020.

[5] Y. Abe, T. Nishimura, and A. Yamada, "Optimum electrical and optical properties of TCO for Cu(In,Ga)Se_2 PV module applications," *Physica Status Solidi*, vol. 221, no. 3, Oct. 2023, Art. no. 2300641, doi: 10.1002/pssa.202300641.

[6] J.-H. Siew, Y.-H. Chen, Y.-L. Chang, C.-H. Lai, and T.-Y. Lin, "Heat soaking for improving rollover from S at the back of CIGSSe solar cells," *IEEE J. Photovolt.*, vol. 13, no. 4, pp. 503–509, Jul. 2023, doi: 10.1109/JPHOTOV.2023.3271891.

[7] K. Fai Tai et al., "Characterization of the back contact of CIGS solar cell as the origin of 'rollover' effect," pp. 237–250, Jun. 2016, doi: 10.4229/EUPVSEC20162016-3AO.5.3.

[8] K. J. Hsiao, J. D. Liu, H. H. Hsieh, and T. S. Jiang, "Electrical impact of $MoSe_2$ on CIGS thin-film solar cells," *Phys. Chem. Chem. Phys.*, vol. 15, no. 41, pp. 18174–18178, Nov. 2013, doi: 10.1039/c3cp53310g.

[9] X. Zhang, D. Zhuang, L. Zhang, M. Zheng, and Y. Wang, "Improvement of Ag(In,Ga)Se_2/Mo interface and solar cell performance by preselenization of the Mo back contact," *IEEE J. Photovolt.*, vol. 10, no. 6, pp. 1900–1907, Nov. 2020, doi: 10.1109/JPHOTOV.2020.2983258.

[10] X. Zhang, M. Kobayashi, and A. Yamada, "Comparison of Ag(In,Ga)Se_2/Mo and Cu(In,Ga)Se_2/Mo interfaces in solar cells," *ACS Appl. Mater. Interfaces*, vol. 9, no. 19, pp. 16215–16220, Apr. 2017, doi: 10.1021/acsami.7b02548.

[11] D. Abou-Ras et al., "Formation and characterisation of $MoSe_2$ for Cu(In,Ga)Se_2 based solar cells," *Thin Solid Films*, vol. 480–481, pp. 433–438, Jun. 2005, doi: 10.1016/j.tsf.2004.11.098.

[12] T. Böker et al., "Band structure of MoS_2, $MoSe_2$, and α – $MoTe_2$: Angle-resolved photoelectron spectroscopy and ab initio calculations," *Phys. Rev. B Condens. Matter. Mater. Phys.*, vol. 64, no. 23, Nov. 2001, Art. no. 235305, doi: 10.1103/PhysRevB.64.235305.

[13] F. S. Hasoon and H. A. Al-Thani, "The formation of the $MoSe_2$ layer at Mo/CIGS interface and its effect on the CIGS device performance," in *Proc. IEEE 43rd Photovoltaic Spec. Conf.*, 2016, pp. 1469–1473, doi: 10.1109/PVSC.2016.7749861.

[14] Y. C. Lin, M. T. Shen, Y. L. Chen, H. R. Hsu, and C. H. Wu, "A study on $MoSe_2$ layer of Mo contact in Cu(In,Ga)Se_2 thin film solar cells," *Thin Solid Films*, vol. 570, Part B, pp. 166–171, Nov. 2014, doi: 10.1016/j.tsf.2014.04.016.

[15] T. Wada, N. Kohara, S. Nishiwaki, and T. Negami, "Characterization of the Cu(In,Ga)Se_2/Mo interface in CIGS solar cells," *Thin Solid Films*, vol. 387, no. 1–2, pp. 118–122, May 2001, doi: 10.1016/S0040-6090(00)01846-0.

[16] M. Burgelman, P. Nollet, and S. Degrave, "Modelling polycrystalline semiconductor solar cells," *Thin Solid Films*, vol. 361–362, pp. 527–532, Feb. 2000, doi: 10.1016/S0040-6090(99)00825-1.

[17] Y. Song et al., "Self-organized back surface field to improve the performance of $Cu_2ZnSn(S,Se)_4$ solar cells by applying P-type $MoSe_2$:Nb to the back electrode interface," *ACS Appl. Mater. Interfaces*, vol. 11, no. 35, pp. 31851–31859, Sep. 2019, doi: 10.1021/acsami.9b08946.

[18] Y. Zhu et al., "Controllable 2H/3R phase transition and conduction behavior change in $MoSe_2$:Nb substitution by high pressure synthesis for promising thermoelectric conversion," *Appl. Phys. Lett.*, vol. 122, no. 13, Mar. 2023, Art. no. 133903, doi: 10.1063/5.0141999.

[19] T. Nishimura et al., "P-type Nb-doped MoS_2 layer for solar cell application," *Physica Status Solidi - Rapid Res. Lett.*, vol. 17, no. 2, Feb. 2023, Art. no. 2200236, doi: 10.1002/pssr.202200236.

[20] T. Nishimura, S. Toki, H. Sugiura, K. Nakada, and A. Yamada, "Interfacial quality improvement of Cu(In,Ga)Se_2 thin film solar cells by Cu-depletion layer formation," *Appl. Phys. Exp.*, vol. 9, no. 9, Sep. 2016, Art. no. 092301, doi: 10.7567/APEX.9.092301.

[21] J. Keller et al., "Wide-gap (Ag,Cu)(In,Ga)Se_2 solar cells with different buffer materials—A path to a better heterojunction," *Prog. Photovolt.*, vol. 28, no. 4, pp. 237–250, Apr. 2020, doi: 10.1002/pip.3232.

[22] T. Nishimura, S. Toki, H. Sugiura, K. Nakada, and A. Yamada, "Effect of Cu-deficient layer formation in Cu(In,Ga)Se_2 solar-cell performance," *Prog. Photovolt.*, vol. 26, no. 4, pp. 291–302, Apr. 2018, doi: 10.1002/pip.2972.

[23] T. Nishimura, K. Nakada, and A. Yamada, "Examination of a Cu-deficient layer on Cu(In, Ga)Se_2 films fabricated by a three-stage process for highly efficient solar cells," *ACS Appl. Energy Mater.*, vol. 2, no. 7, pp. 5103–5108, Jun. 2019, doi: 10.1021/acsaem.9b00774.

[24] T. Maeda, W. Gong, and T. Wada, "$CuInSe_2$, $CuIn_3Se_5$, and $CuIn_5Se_8$ phases in Cu-poor Cu_2Se–In_2Se_3 pseudo-binary system—Their crystal structures, optical properties and electronic structures," *Curr. Opin. Green Sustain. Chem.*, vol. 4, pp. 77–83, Apr. 2017, doi: 10.1016/j.cogsc.2017.03.004.

[25] K. K. Kam and B. A. Parkinson, "Detailed photocurrent spectroscopy of the semiconducting group VI transition metal dichalcogenides," *J. Phys. Chem.*, vol. 86, no. 4, pp. 463–467, Feb. 1982, doi: 10.1021/j100393a010.

[26] Z. Lin, H. Yan, J. Liu, and Y. An, "Defects engineering monolayer $MoSe_2$ magnetic states for 2D spintronic device," *J. Alloys. Compd*, vol. 774, pp. 160–167, Feb. 2019, doi: 10.1016/j.jallcom.2018.09.353.

[27] M. Bär et al., "Electronic level alignment at the deeply buried absorber/Mo interface in chalcopyrite-based thin film solar cells," *Appl. Phys. Lett.*, vol. 93, no. 4, 2008, Art. no. 042110, doi: 10.1063/1.2955532.

[28] M. Moustafa, T. AlZoubi, S. Yasin, Z. A. Waar, and A. Moghrabi, "Towards high-efficiency CZTSe solar cells through the optimization of the p-$MoSe_2$ interfacial layer," *J. Phys. Conf. Ser.*, vol. 2022, no. 1, Oct. 2021, Art. no. 012022, doi: 10.1088/1742-6596/2022/1/012022.

[29] C. Zhang et al., "Numerical study to improve the back interface contact of CZTSSe solar cells using Oxygen-doped $Mo(Se_{1-x}, O_x)_2$," *J. Phys. Chem. C*, vol. 125, no. 30, pp. 16746–16752, Jul. 2021, doi: 10.1021/acs.jpcc.1c04129.

[30] F. 'Izzati Za'abar et al., "A numerical investigation on the combined effects of $MoSe_2$ interface layer and graded bandgap absorber in cigs thin film solar cells," *Coatings*, vol. 11, no. 8, Aug. 2021, Art. no. 930, doi: 10.3390/coatings11080930.

[31] H. yu Sun, P. hai Li, Y. ming Xue, Z. xiang Qiao, and L. Sai, "Effect of $MoSe_2$ on the performance of CIGS solar cells," *Optoelectron. Lett.*, vol. 15, no. 6, pp. 428–434, Nov. 2019, doi: 10.1007/s11801-019-9027-z.

[32] Y. Ma et al., "Electronic and magnetic properties of perfect, vacancy-doped, and nonmetal adsorbed $MoSe_2$, $MoTe_2$ and WS_2 monolayers," *Phys. Chem. Chem. Phys.*, vol. 13, no. 34, pp. 15546–15553, Sep. 2011, doi: 10.1039/c1cp21159e.

[33] Y. Zhao et al., "High response and broadband photodetection by monolayer $MoSe_2$ with vanadium doping and Mo vacancies," *Appl. Surf. Sci.*, vol. 564, Oct. 2021, Art. no. 150399, doi: 10.1016/j.apsusc.2021.150399.

[34] D. Gao et al., "Dual-native vacancy activated basal plane and conductivity of $MoSe_2$ with high-efficiency hydrogen evolution reaction," *Small*, vol. 14, no. 14, Feb. 2018, Art. no. 1704150, doi: 10.1002/smll.201704150.

[35] M. Cardona and L. Ley, "Methods to determine the work function," in *Photoemission in Solids I*, 1st ed. Heidelberg, Germany: Springer, 1978, Art. no. 19.

[36] J. Verschraegen and M. Burgelman, "Numerical modeling of intraband tunneling for heterojunction solar cells in SCAPS," *Thin Solid Films*, vol. 515, no. 15, pp. 6276–6279, May 2007, doi: 10.1016/j.tsf.2006.12.049.

[37] K. Yang, J. R. East, and G. I. Haddad, "Numerical modeling of abrupt heterojunctions using a thermionic-field emission boundary condition," *Solid-State Electron.*, vol. 36, no. 3, pp. 321–330, Mar. 1993, doi: 10.1016/0038-1101(93)90083-3.

[38] T. Nishimura and A. Yamada, "Optimum back junction utilizing P-type $MoSe_2$:Nb layer for Cu(In,Ga)Se_2 solar cells," in *Proc. 33rd Int. Photovolt. Sci. Eng. Con.*, Nov. 2022, pp. 31851–31859.

[39] J. Zhang et al., "Niobium and rhenium doping in $MoSe_2$ monolayer during molecular beam epitaxy: Shallow dopants and defect proliferation," *APL Mater*, vol. 11, no. 7, Jul. 2023, Art. no. 071113, doi: 10.1063/5.0152247.